InterPore JOURNAL

Supplementary Material

A HYDRO-GEOMECHANICAL POROUS-MEDIA MODEL TO STUDY EFFECTS OF ENGINEERED CARBONATE PRECIPITATION IN FAULTS

Yue Wang*, Holger Class*

*Institute for Modelling Hydraulic and Environmental Systems, Department of Hydromechanics and Modelling of Hydrosystems, University of Stuttgart, Stuttgart, Germany; *These authors contributed equally to this work*

1. APPENDIX A: EFFECTIVE POROSITY

$$\Delta\phi = -\frac{\alpha-\phi}{K}\Delta p \tag{A1}$$

$$\Delta\phi = -(\frac{1-\phi}{K}-\frac{1}{K_s})(-K\epsilon+(\alpha-1)p_{eff})$$

$$\Delta\phi = (1-\phi-\frac{K}{K_s})\epsilon+(\frac{1-\phi}{K}-\frac{1}{K_s})\frac{K}{K_s}p_{eff}$$

$$\Delta\phi = \alpha\epsilon-\phi\epsilon+(\frac{1}{K_s}-\frac{\phi}{K_s}-\frac{K}{K_s^2})p_{eff}$$

$$\Delta\phi == \alpha\epsilon+(\frac{1}{K_f}+\frac{1}{K_s}-\frac{\phi}{K_s}-\frac{K}{K_s^2})p_{eff}$$

$$\Delta\phi = \alpha\epsilon+\frac{1}{M}p_{eff},$$

Here $\epsilon = -\frac{\Delta V}{V} = -\frac{\Delta V_p}{V_p} = \frac{p_{eff}}{K_f}$, with K_f as the effective bulk modulus of the fluids (pore pressure in response to pore volume change). If only the single phase fluid is present, the formulation is identical to the one in Coussy (1).

2. APPENDIX B: CONSTANT CEMENT MODEL

Phase 1: $\phi_c \rightarrow \phi_b$

$$K = \frac{n(1-\phi_c)M_cS_n}{6} \tag{B2}$$

$$G_= \frac{3K_{\mathrm{dry}}}{5}+\frac{3n(1-\phi_c)G_cS_\tau}{20} \tag{B3}$$

Here the coefficients S_n and S_τ are determined by specific equations that take into account the elastic moduli of the grain material and cement material, critical porosity, as well as various statistical parameters.

 https://doi.org/10.69631/ipj.v2i2nr41

$$S_n = A_n(\Lambda_n)\alpha^2 + B_n(\Lambda_n)\alpha + C_n(\Lambda_n) \quad \text{(B4)}$$

$$A_n(\Lambda_n) = -0.024153\Lambda_n^{-1.3646} \quad \text{(B5)}$$

$$B_n(\Lambda_n) = 0.20405\Lambda_n^{-0.89008} \quad \text{(B6)}$$

$$C_n(\Lambda_n) = 0.00024649\Lambda_n^{-1.9864} \quad \text{(B7)}$$

$$S_\tau = A_\tau(\Lambda_\tau, \nu_s)\alpha^2 + B_\tau(\Lambda_\tau, \nu_s)\alpha + C_\tau(\Lambda_\tau, \nu_s) \quad \text{(B8)}$$

$$A_\tau(\Lambda_\tau, \nu_s) = -10^{-2}(2.26\nu_s^2 + 2.07\nu_s + 2.3)\Lambda_\tau^{0.079\nu_s^2+0.1754\nu_s-1.342} \quad \text{(B9)}$$

$$B_\tau(\Lambda_\tau, \nu_s) = (0.0573\nu_s^2 + 0.0937\nu_s + 0.202)\Lambda_\tau^{0.0274\nu_s^2+0.0529\nu_s-0.8765} \quad \text{(B10)}$$

$$C_\tau(\Lambda_\tau, \nu_s) = 10^{-4}(9.654\nu_s^2 + 4.945\nu_s + 3.1)\Lambda_\tau^{0.01867\nu_s^2+0.4011\nu_s-1.8186} \quad \text{(B11)}$$

$$\Lambda_n = \frac{2G_c(1-\nu_s)(1-\nu_c)}{\pi G_s(1-2\nu_c)} \quad \text{(B12)}$$

$$\Lambda_\tau = \frac{G_c}{\pi G_s} \quad \text{(B13)}$$

$$\alpha = \left[\frac{\frac{2}{3}(\phi_c - \phi)}{1-\phi_c}\right]^{0.5} \quad \text{(B14)}$$

$$\nu_c = 0.5\frac{(\frac{K_c}{G_c} - \frac{2}{3})}{(\frac{K_c}{G_c} + \frac{1}{3})} \quad \text{(B15)}$$

$$\nu_s = 0.5\frac{(\frac{K_s}{G_s} - \frac{2}{3})}{(\frac{K_s}{G_s} + \frac{1}{3})} \quad \text{(B16)}$$

Phase 2: $\phi_b \to 0$ K_b and G_b are bulk modulus and shear modulus calculated after pre-listed equations. Bulk and shear moduli are then interpolated using HS lower bound.

$$K = \left[\frac{\frac{\phi}{\phi_b}}{K_b + \frac{4}{3}G_b} + \frac{1-\frac{\phi}{\phi_b}}{K_s + \frac{4}{3}G_b}\right]^{-1} - \frac{4}{3}G_b \quad \text{(B17)}$$

$$G = \left[\frac{\frac{\phi}{\phi_b}}{G_b + z} + \frac{1-\frac{\phi}{\phi_b}}{G_s + z}\right]^{-1} - z \quad \text{(B18)}$$

with

$$z = \frac{G_b}{6}\left(\frac{9K_b + 8\mu_b}{K_b + 2\mu_b}\right) \quad \text{(B19)}$$

3. APPENDIX C: COMPARISON WITH COLUMN EXPERIMENT

In this section, we describe our approach to completing the simulation and comparing the results with experimental data.

The sand column was simulated for the state after mineralization process, with an assumption of axial symmetric porosity throughout. Since the Unconfined Compressive Strength (UCS) test was conducted under dry conditions, fluid effects were neglected, simplifying the simulation to purely elastic behavior.

Given the axial symmetry of the column, we reduced the simulation to a 2D domain. This 2D domain has dimensions of 25 mm radius by 100 mm height along the axis.

To calculate the momentum balance, we employed the following balance equation expressed in cylindrical coordinates:

$$\frac{1}{r}\frac{\partial r\sigma_r}{\partial r}+\frac{\partial \tau_{zr}}{\partial z}-\frac{1}{r}\sigma_\theta=0 \qquad \text{(C20)}$$
$$\frac{1}{r}\frac{\partial r\tau_{zr}}{\partial r}+\frac{\partial \sigma_z}{\partial z}=0,$$

where σ_r, σ_z are the normal stress along radius and axis and τ_{zr} for the shear stress. The stress-strain relationship can be determined using Hooke's Law, where the elastic moduli E, ν are determined by cementation model

$$\begin{pmatrix}\sigma_r\\ \sigma_z\\ \sigma_\theta\\ \tau_{rz}\end{pmatrix}=\frac{E}{(1+\nu)(1-2\nu)}\begin{pmatrix}1-\nu & \nu & \nu & 0\\ \nu & 1-\nu & \nu & 0\\ \nu & \nu & 1-\nu & 0\\ 0 & 0 & 0 & \frac{1-2\nu}{2}\end{pmatrix}\begin{pmatrix}\varepsilon_r\\ \varepsilon_z\\ \varepsilon_\theta\\ \gamma_{rz}\end{pmatrix} \qquad \text{(C21)}$$

with strain given by

$$\begin{pmatrix}\varepsilon_r\\ \varepsilon_\theta\\ \varepsilon_z\\ \gamma_{rz}\end{pmatrix}=\begin{pmatrix}\frac{\partial}{\partial r} & 0\\ \frac{1}{r} & 0\\ 0 & \frac{\partial}{\partial z}\\ \frac{\partial}{\partial z} & \frac{\partial}{\partial r}\end{pmatrix}\begin{pmatrix}u_r\\ u_z\end{pmatrix} \qquad \text{(C22)}$$

The boundary condition is set as follows, with a given loading velocity.

Table C1: Boundary Conditions for $\mathbf{u_r}$ and $\mathbf{u_z}$

Boundary	u_r	u_z
Top	no stress	-0.045 * t
Bottom	no stress	0
Inner	0	no stress
Outer	no stress	no stress

We calculate the average normal stress in the top cells at each time step to determine the loading pressure, allowing us to generate the stress-strain diagram shown in **Figure 6** in the main text.

4. Appendix D: Additional results of the showcase

Figure D1 illustrates the evolution of pore pressure in the injection area, clearly divided into two distinct phases separated by the cessation of injection. The first phase corresponds to the injection period, characterized by a continuous increase in pore pressure. In the second phase, pore pressure gradually decreases as a result of pressure diffusion driven by fluid migration. Concurrently, gas saturation declines very slowly due to capillary effects.

Figure D2 illustrates the pore pressure distribution along the reservoir at a depth of 1550 m for three studied cases. Two clear discontinuities in the pressure profiles highlight the influence of fault zones. The left fault, characterized by lower permeability (sealed fault), restricts fluid movement, resulting in a moderate pressure drop across this fault. Furthermore, the permeability of the fault significantly affects the rate at which pore pressure rises during injection. In contrast, beyond the second fault (on the right),

the effect of injection diminishes considerably, owing to its higher permeability and proximity to a pressure boundary that enables rapid fluid drainage. The central region of each plot demonstrates a delayed pore-pressure response following injection cessation, where the pore pressure continues to rise

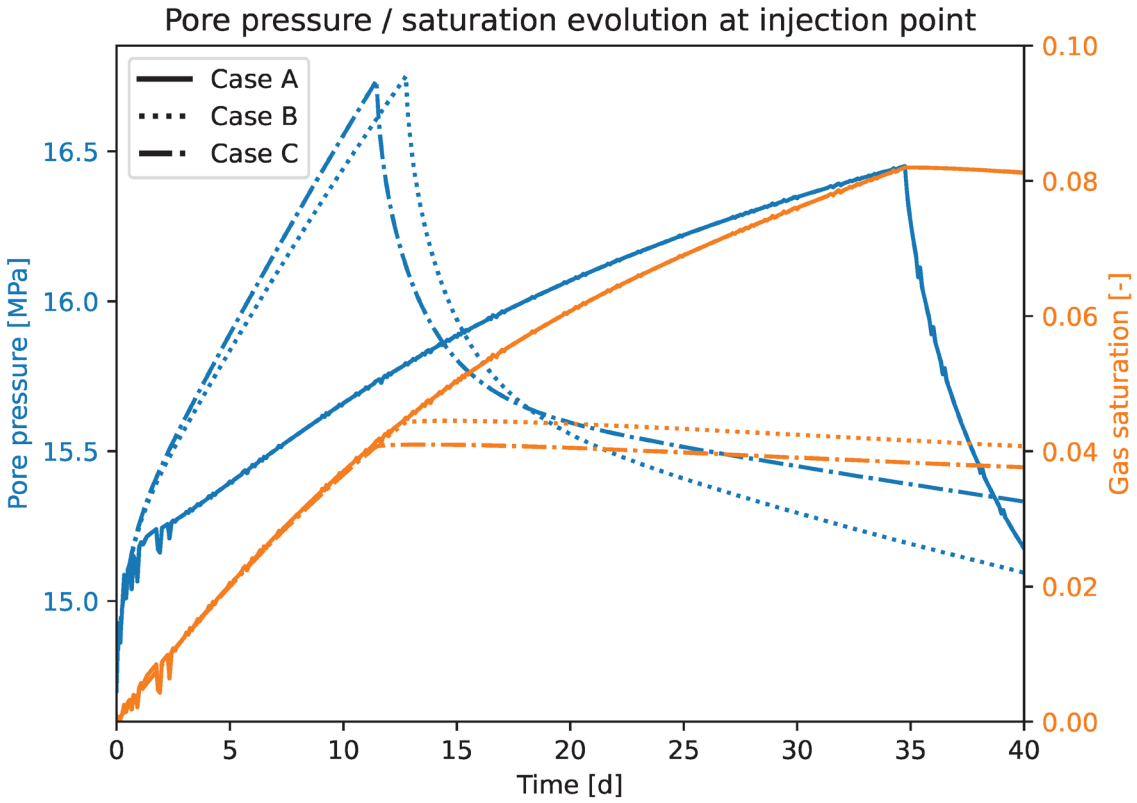

Figure D1: Time evolution of pore pressure and gas saturation in the injection zone for the three cases.

briefly after injection ends before gradually decreasing due to pressure diffusion processes. Additionally, the slope direction observed in this central area reflects the coupled hydro-mechanical behavior: the stresses induced by injection are partially equilibrated by changes in pore pressure governed by reservoir boundary conditions.

The evolution of the safety margin along both fault zones is presented in **Figure D3** and **Figure D4**. The sealing (closure) condition of the left fault zone produces a distinctly different evolution pattern compared to the right fault. Both figures clearly demonstrate areas approaching shear failure, as indicated by the safety margin decreasing towards zero. Notably, regions characterized by stiffer rock properties are more prone to reaching failure conditions, underscoring the critical role of mechanical heterogeneity in controlling fault stability. Additionally, **Figure D5** illustrates the variation in shear stress induced by injection for Case B, highlighting that increased shear stress predominantly develops along fault and rock zones, coinciding precisely with areas exhibiting significant mechanical heterogeneity.

 https://doi.org/10.69631/ipj.v2i2nr41

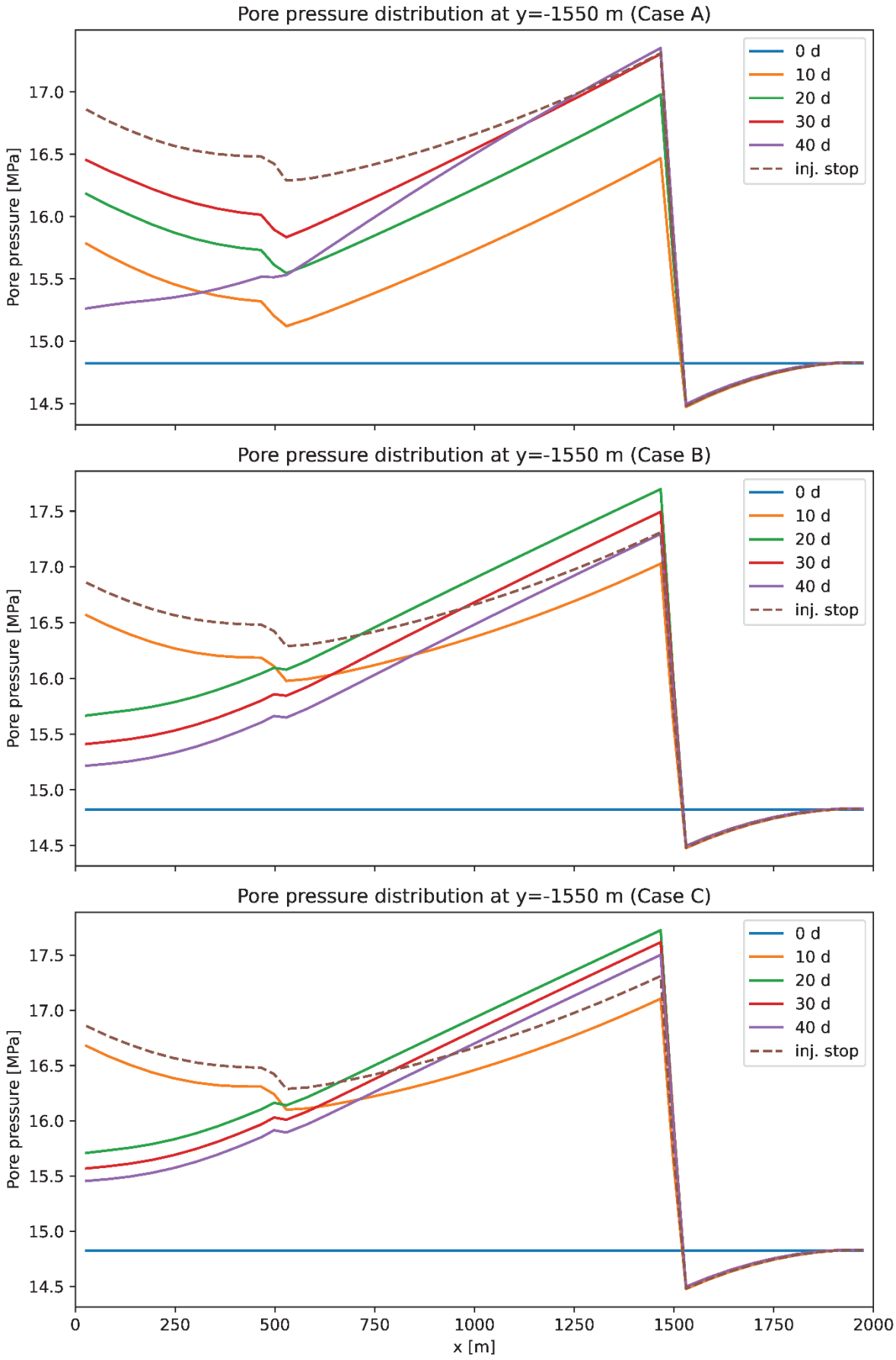

Figure D2: Pore pressure distribution at a depth of 1550 m for the three cases.

 https://doi.org/10.69631/ipj.v2i2nr41

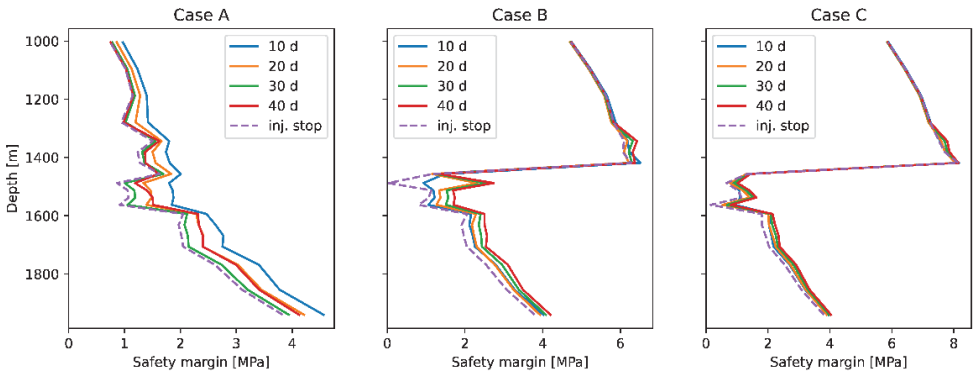

Figure D3: Time evolution of the safety margin in the left fault zone for the three cases.

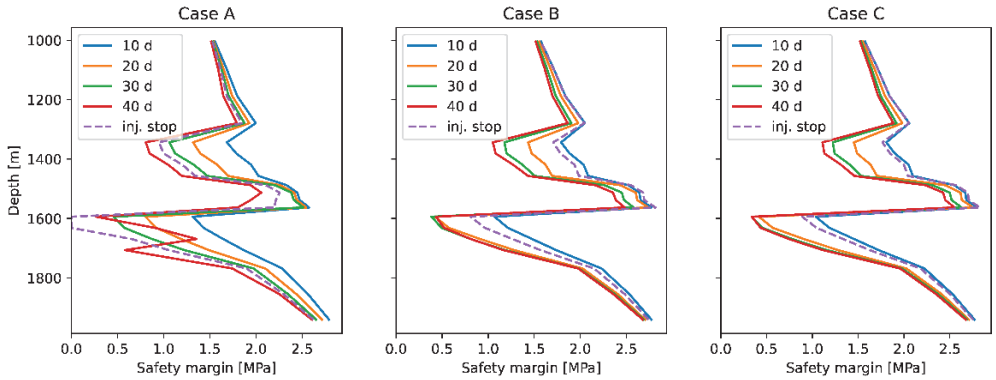

Figure D4: Time evolution of the safety margin in the right fault zone for the three cases.

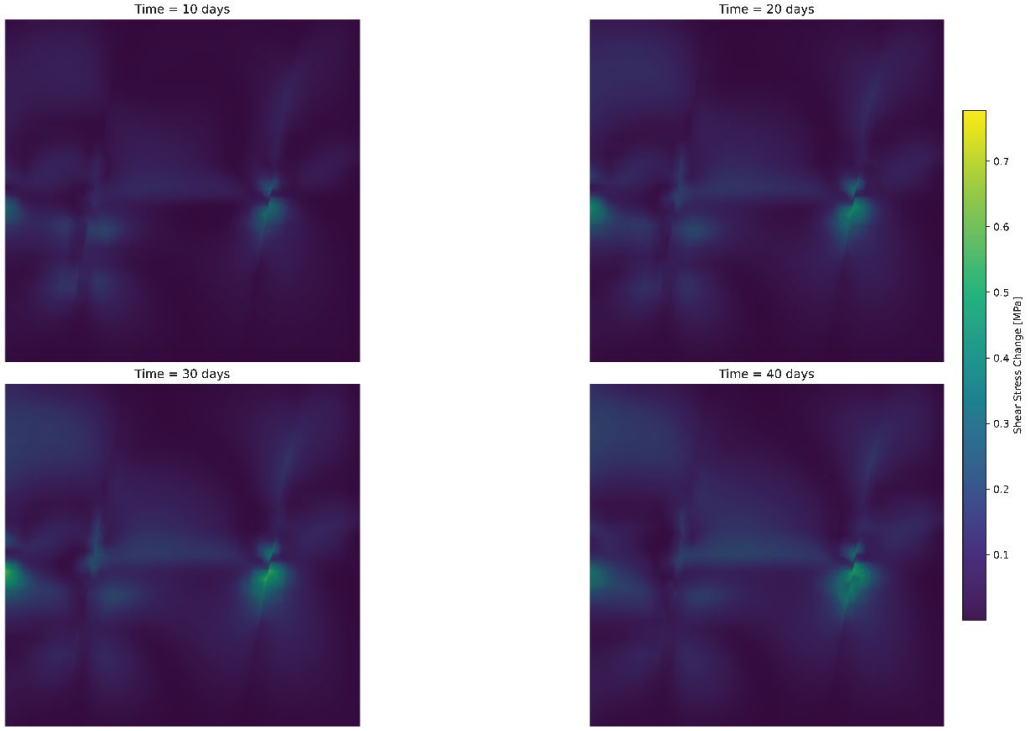

Figure D5: Time evolution of the shear stress change in the domain for the three cases.

Reference

1. Coussy, Olivier. 2003. *Poromechanics*. Wiley. https://doi.org/10.1002/0470092718.